

# Stabilization of Tetragonal HfO<sub>2</sub> under Low Active Oxygen Source Environment in Atomic Layer Deposition

Deok-Yong Cho,<sup>\*,†</sup> Hyung Suk Jung,<sup>‡</sup> Il-Hyuk Yu,<sup>‡</sup> Jung Ho Yoon,<sup>‡</sup> Hyo Kyeom Kim,<sup>‡</sup> Sang Young Lee,<sup>‡</sup> Sang Ho Jeon,<sup>‡</sup> Seungwu Han,<sup>‡</sup> Jeong Hwan Kim,<sup>‡</sup> Tae Joo Park,<sup>§</sup> Byeong-Gyu Park,<sup>||</sup> and Cheol Seong Hwang<sup>\*,‡</sup>

<sup>†</sup>IWE2 & JARA-FIT, RWTH Aachen University, D-52056, Aachen, Germany

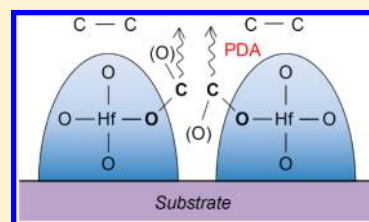
<sup>‡</sup>WCU Hybrid Materials Program, Department of Materials Science and Engineering and Inter-University Semiconductor Research Center, Seoul National University, Seoul, 151-744, Korea

<sup>§</sup>Department of Materials Engineering, Hanyang University, Ansan, 426-791, Korea

<sup>||</sup>Pohang Light Source, Pohang University of Science and Technology, Pohang, 790-784, Korea

**ABSTRACT:** The structural and electronic properties of HfO<sub>2</sub> thin films grown by atomic layer deposition (ALD) under various ozone concentrations were investigated using X-ray diffraction (XRD), photoemission (XPS), reflectometry (XRR), and absorption spectroscopy (XAS) and their fine structure (XAFS) analysis. It was found that in the as-grown states, the oxygen stoichiometry and local atomic structure in amorphous HfO<sub>2</sub> domains are maintained nearly as constants even when the film is grown without external ozone supply, while some C–O bonds remain between the almost stoichiometric HfO<sub>2</sub> domains due to incomplete oxidation of the precursors. After a postdeposition annealing (PDA), the films crystallize with a monoclinic structure (*P*<sub>2</sub><sub>1</sub>/*c*), except for the case of the no-ozone supply in which the film possesses a tetragonal crystal structure (*P*<sub>4</sub><sub>2</sub>/*nmc*). It is demonstrated that the carbonate bonds play a major role in stabilizing the tetragonal structure through nanoscale separation of the HfO<sub>2</sub> domains. Accordingly, the roles of the oxygen source and the PDA are also newly addressed as being related to the carbonate bonds. The ozone gas acts as an oxygen supplier, and more importantly, it reduces the residual carbonates to stabilize the bulk crystal structure in the thin films. The PDA not only delivers the thermal energy to induce the crystallization but also eliminates C atoms to increase the size of the HfO<sub>2</sub> domains leading to the densification of the films.

**KEYWORDS:** atomic layer deposition, HfO<sub>2</sub>, tetragonal, ozone, annealing, carbonate



## 1. INTRODUCTION

With recent advent of the era of high-permittivity (*k*)-oxide-based field effect transistors (FET), it has been a promising endeavor to study the electrochemical properties of the high-*k* oxides.<sup>1</sup> For the mass production of the high-*k* oxide layers, the atomic layer deposition (ALD) technique now has been adopted in industry.<sup>2–4</sup> The figure of merit of the high-*k* oxides in actual devices, such as a leakage current or permittivity, has been examined widely, with various control parameters (see, for example, refs 5–8). So far, it is known that the electrical performances of the high-*k* gate stack scatter quite strongly depending on the chemistry or atomic structure in the oxide or at the interfaces with metal electrodes.<sup>9</sup> Therefore, there still remains the fundamental task of understanding the influences of the processes in the ALD on the chemistry and atomic structures in the high-*k* gate oxide itself.

As for the growth of binary oxides, the ALD cycle consists of four steps: (1) chemical adsorption of metal precursors, (2) purging the superfluous metal precursors, (3) removal of ligands and oxidation of the metal atoms (or ions) by oxygen source gas, and (4) purging the excessive oxygen source gas. The role of each step appears to be evident as has been demonstrated in many studies.<sup>3,4</sup> Among them, the most

important process in regard to the chemistry of the oxide film is perhaps the oxidation process, since the ionic valences would vary significantly depending on the status of the ligand substitutions, while the other processes may have relatively less crucial influences.<sup>10</sup> It is undoubtedly clear that the concentration of the oxygen source should be closely related to the actual oxygen contents in the films. However, this does not mean that the role of oxygen source is completely understood. If the films are not fully oxidized, some fragments of ligands should remain because of incomplete substitution by the oxygen source.<sup>11–14</sup> The remaining atomic species other than those from the target oxides could also influence the atomic structure and chemistry of the film, leading to the complexity in the roles of the oxygen source.<sup>15–17</sup> Meanwhile, a thermal treatment is frequently applied after the ALD cycles to enhance the crystallinity or reduce the number of defects (“healing”).<sup>18,19</sup> The effects of the postdeposition annealing (PDA) also could be complicated by the remaining atomic species (from the insufficient oxidation), since they could migrate

**Received:** January 12, 2012

**Revised:** July 12, 2012

**Published:** August 27, 2012



during the PDA.<sup>19,20</sup> Therefore, it is worthy to study the influences of the oxygen source concentration and the PDA on the structural and electronic properties of the ALD high-*k* films. Although there have been several reports on this subject,<sup>11–13,15,19</sup> detailed understanding of the roles of the remaining atomic species in the high-*k* film depending on the oxygen source concentration has been missing.

In this work, hafnium oxide (HfO<sub>2</sub>) was chosen as a representative oxide system, since it is most generally used as the high-*k* gate dielectric to date.<sup>21,22</sup> A comprehensive study on the evolution of the structural and electronic properties under different oxygen source concentrations and the PDA was performed using various X-ray techniques, such as diffraction/reflectometry, photoemission, and absorption spectroscopy. It is found that in an extreme strong oxidant-deficient condition, the HfO<sub>2</sub> film undergoes a structural change to a tetragonal structure after the PDA. The stabilization of the tetragonal structure is correlated with carbonate bonds that remain because of the insufficient precursor oxidation, which would influence the grain size of crystallized film eventually; the smaller grain size would result in the tetragonal phase due to its lower grain boundary energy. The roles of the oxygen source and the PDA are newly suggested as being related to the carbonate bonds.

## 2. SAMPLE PREPARATION AND MEASUREMENTS

All the HfO<sub>2</sub> films were deposited on HF-cleaned Si wafers by atomic layer deposition (ALD) at 280 °C. Hf[N(C<sub>2</sub>H<sub>5</sub>)(CH<sub>3</sub>)<sub>2</sub>]<sub>4</sub> was used as the Hf precursor, and ozone was used as the oxygen source. Ozone gas was generated by a flowing mixture gas of O<sub>2</sub> (1,350 standard cubic centimeters per min; sccm) and N<sub>2</sub> (10 sccm) into an ozone generator (Astex, AX8200). The ozone concentrations were chosen as null (only molecular oxygen gas flow), 70 g/m<sup>3</sup>, 170 g/m<sup>3</sup> (known as standard), and 280 g/m<sup>3</sup>. The ALD was performed for 130 cycles, resulting in a range of film thickness of 13 ± 1 nm. The difference in the film thicknesses does not affect the main analyses in this work. Details of the ALD processes were reported elsewhere.<sup>23</sup> It is the major topic of this work that the structural properties and electronic structure of the films grown without ozone gas are different from those of the standard film (with ozone concentration of 170 g/m<sup>3</sup>) but not necessarily very inferior (for example, see Figure 7 to compare the conduction bands). However, a high leakage current was observed in the electrical measurement; the leakage current density (*J<sub>g</sub>*) in a thinner (6 nm-thick) gate/channel structure, exceeds 1 A/cm<sup>2</sup> at a voltage of -1.0 V in the case of no-ozone sample after annealing, which, in contrast, remains below 10<sup>-4</sup> A/cm<sup>2</sup> in the case of 70, 170, and 280 g/m<sup>3</sup> samples. Also, the capacitance could not be measured due to the high *J<sub>g</sub>* in the case of no-ozone sample. As will be discussed later, this should be attributed to the formation of conducting carbon-containing channels between some HfO<sub>2</sub> domains rather than the significant degradation of the HfO<sub>2</sub> domains themselves.<sup>21</sup> The postdeposition annealing (PDA) was performed in an N<sub>2</sub> environment (100 Torr) at 550 °C for 1 min. The role of the PDA is also studied in this work.

The glancing angle X-ray diffraction (GAXRD) was performed in order to examine the crystallinities using a PANalytical X'Pert diffractometer equipped with a monochromatic Cu Kα<sub>1</sub> source. The film density was measured by X-ray reflectometry (XRR) in the same apparatus. The chemistry of the samples was examined by X-ray photoelectron spectroscopy (XPS) using a Sigma Probe (ThermoVG) system equipped with a monochromatic Al Kα sources. The angle between the source and the analyzer was 90°. The film surfaces were not cleaned in order to avoid possible compositional or structural changes at the surface caused by etching. The sample charging effect was prevented by monitoring the binding energy shifts by tuning the flux of incident X-rays. The local atomic structures and electronic structures were examined by performing the Hf L<sub>3</sub>-edge and O K-edge X-ray absorption spectroscopies (XAS) at 3C1 and 2A beamlines in

the Pohang Light Source (Korea) in fluorescence yield mode and in a total electron yield mode, respectively. All the measurements were done at room temperature. The microstructures of the crystallized films after the PDA were estimated by the cross-section high-resolution transmission electron microscopy (HRTEM).

## 3. RESULTS

The glancing angle X-ray diffraction (GAXRD) manifests the formation of a tetragonal phase in HfO<sub>2</sub> film after PDA when the sample is grown without an ozone supply (section 3.1). The accompanying changes in local atomic structures are also verified in the Hf L<sub>3</sub>-edge extended X-ray absorption fine structure (EXAFS) analysis and O K-edge X-ray absorption spectroscopy (XAS; sections 3.2 and 3.3). The core-level X-ray photoelectron spectroscopy (XPS) shows the existence of C–O bonds in the HfO<sub>2</sub> films, which will be correlated to the formation of the tetragonal phase in section 3.4. The resultant decrease in film density, observed in X-ray reflectometry (XRR), will be discussed in section 3.5. Finally, the consequent changes in valence and conduction bands will be discussed in section 3.6.

**3.1. XRD.** Figure 1 shows the GAXRD patterns of the HfO<sub>2</sub> films grown under different ozone concentrations: 0, 70, 170,

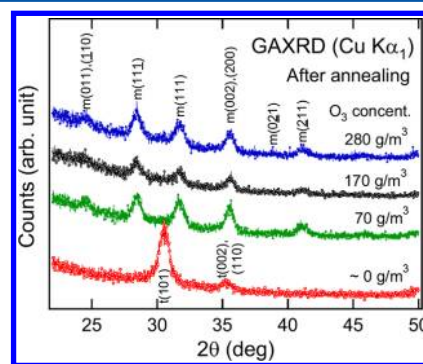


**Figure 1.** Cu Kα<sub>1</sub> glancing angle X-ray diffraction (GAXRD) patterns of the HfO<sub>2</sub> films grown under different ozone concentrations: 0, 70, 170, and 280 g/m<sup>3</sup> after annealing. Clear signatures of the tetragonal crystal structure are shown in the case of the no-ozone sample.

and 280 g/m<sup>3</sup>. The incident angle of X-rays to the film surface was set to be 2°. The as-grown samples showed no features except slightly declining background slopes reflecting their amorphous nature, so they are omitted. Meanwhile, the samples after PDA showed clear peaks reflecting their crystalline phases. It is clearly shown that the diffraction patterns of 70, 170, and 280 g/m<sup>3</sup> are similar, while that of ~0 g/m<sup>3</sup> is quite different from the other three samples. The peaks of the first three samples (70, 170, and 280 g/m<sup>3</sup>) can be assigned according to a monoclinic crystal structure (*P2<sub>1</sub>/c*), consistent to the former knowledge that HfO<sub>2</sub> films prefers to form the monoclinic structure.<sup>24</sup> In contrast, those of the latter (~0 g/m<sup>3</sup>) can be assigned to a tetragonal crystal structure, since they are quite similar to the diffraction patterns of tetragonal HfO<sub>2</sub> (*P4<sub>2</sub>/nmc*).<sup>25,26</sup> Absence of features near the angle of 2θ = 40° indicates that an orthorhombic phase is not contained in this sample.<sup>27,28</sup> The lattice constants deduced from the 2θ of the main peaks (101) and (002), were *a* = 3.45 Å and *c* = 4.94 Å, which are slightly lower values than the respective lattice constants of tetragonal HfO<sub>2</sub> by ~3%. The contraction of the lattice compared to tetragonal HfO<sub>2</sub> might reflect the formation of nanosized crystallites (which will be suggested in section 3.4)

since lack of attractive interactions at the surfaces of the crystallites will lower the lattice constants slightly. However, it does not accompany a noticeable decrease in the Hf–O bond lengths (see section 3.2) because of the movement of the positively charged Hf<sup>4+</sup> ions toward the remaining O<sup>2-</sup> ions<sup>18</sup> nor a change in the chemistry of Hf<sup>4+</sup> or O<sup>2-</sup> ions (see section 3.4).

It is clearly shown in Figure 1 that the HfO<sub>2</sub> film grown under the no-ozone condition has a tetragonal crystal structure after PDA. Because the tetragonal phase generally has higher *k* than the monoclinic phase,<sup>28,29</sup> this growth method might be desirable for high-*k* industry. However, the resultant films are observed to accompany very high leakage currents, so they are not eligible for gate dielectrics, unfortunately. It will be shown in the next section that the local structure of amorphous HfO<sub>2</sub> remains, however, monoclinic-like, even for the sample grown without ozone. This suggests that the local structures of HfO<sub>2</sub> in the as-grown states do *not* solely determine the crystal structures after PDA. Rather, some extrinsic factor other than the HfO<sub>2</sub> itself should be involved to explain the structural discrepancy between the no-ozone samples and the other samples. In section 3.4, this will be correlated to the C–O bonds remaining between the HfO<sub>2</sub> domains due to the insufficient substitution reaction during the oxidation process.

**3.2. Hf L<sub>3</sub>-Edge EXAFS.** The Hf L<sub>3</sub>-edge EXAFS analyses of the HfO<sub>2</sub> films were processed on *k*<sup>3</sup>-weighted oscillation (*k* = 2–11 Å<sup>-1</sup>) using the UWXAFS package.<sup>30</sup> Figure 2 shows the

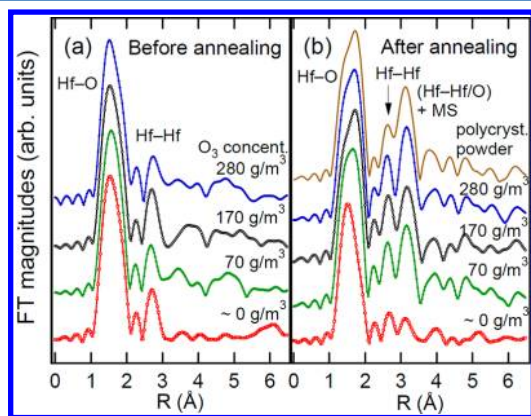


**Figure 2.** Fourier-transformed (FT) extended X-ray absorption fine structures (EXAFS) of the HfO<sub>2</sub> films with various ozone concentrations (a) before and (b) after annealing. The spectrum of a polycrystalline HfO<sub>2</sub> powder is appended for comparison. The difference in line shapes in (b) highlights the discrepancy in local structure in the case of the no-ozone sample after annealing. For more details, see the text.

Fourier-transformed (FT) EXAFS of the HfO<sub>2</sub> films with various ozone concentrations (a) before and (b) after PDA. The features are assigned according to the phase-uncorrected atomic distances *R* values, such as Hf–O, Hf–Hf bonds, or other multiple scattering (MS) features. Overall, the features in Figure 2a are less intense than those in Figure 2b except for the first shell features (Hf–O, *R* ≈ 1.5 Å). Their weaknesses can be attributed to the large structural disorders in the amorphous films, which generally might be more severe in higher *R*.<sup>24</sup> The as-grown films were amorphous, while the films crystallize after the PDA, as was evidenced in Figure 1.

Figure 2a clearly shows the similarity in the Hf–O features irrespective of ozone concentration. This surprisingly suggests

that the oxygen concentration in the HfO<sub>2</sub> film grown under the no-ozone flow condition is not significantly smaller than those in other films; rather, this implies that the Hf atoms are well coordinated by oxygen ions in the ALD process, even without ozone. It should be noted that an O<sub>2</sub> gas was flown into the chamber with a pressure level of a few torr during the oxygen source pulse step, which appears to be enough to oxidize the Hf-precursors.

Nevertheless, the nearly constant number of Hf–O bonds, even without ozone supply, still appears not to be readily acceptable, because according to current knowledge of ALD, there is a certain optimal condition of ozone concentration (e.g., in this apparatus, ~170 g/m<sup>3</sup> for HfO<sub>2</sub> ALD<sup>23</sup>) that guarantees the lowest leakage current at a given dielectric thickness. This contradiction can be resolved by noting that the Hf L<sub>3</sub>-edge EXAFS shown in Figure 2 probes the local structures near the Hf ions only. The films might not be perfectly homogeneous but they do form some amorphous HfO<sub>2</sub> clusters or nanosized “domains” with some other impurities at the boundaries between otherwise more stoichiometric HfO<sub>2</sub> domains. It will be shown in the next section that carbons remain, resulting from insufficient oxidation, indicating that the presence of C–O bonds could be a key factor to trigger the structural transition to the tetragonal phase, which might act as a channel of electrical leakage and could degrade the permittivity of the high-*k* film.<sup>19,31</sup> However, a noticeable difference in the Hf–O coordination could not be observed, even under the intervention of C atoms, since the Hf–O coordination in the HfO<sub>2</sub> nanoclusters were not influenced enough to change noticeably (see Figure 2a).

Interestingly, this similarity does not hold after PDA. Figure 2b shows the FT EXAFS spectra of the four films after PDA as well as that of a polycrystalline HfO<sub>2</sub> powder (with the perfect 7-fold Hf–O coordination) for comparison. The spectra of 70, 170, and 280 g/m<sup>3</sup> samples, overall, are similar to that of the powder sample, reflecting monoclinic crystal structures with similar degrees of crystallinities.<sup>24</sup> Meanwhile, the spectrum of the no-ozone sample is quite different from the other spectra, implying a significant difference in local structures. This clear difference in the case of the no ozone supply is consistent with the tendency in the GAXRD patterns in Figure 1, suggesting that the discrepancy originates from the structural transition. The higher-*R* shells in the spectrum of no-ozone film have lower magnitudes compared with those of other samples in Figure 2b. This can be attributed to the strong influence of the structural disorder, especially on the MS paths,<sup>24</sup> although the intensities of the diffraction peaks of the no-ozone sample are comparable to those of the other samples (see Figure 1).

The FT magnitude (or the area) of the first shell (Hf–O bond) also decreases slightly for the no-ozone sample compared to the other samples after PDA, which appears to be inconsistent with the crystal structure of tetragonal HfO<sub>2</sub> (see section 3.1); in the *P4<sub>2</sub>/nmc* space group, the Hf–O coordination number should be 8, which is larger than the case of monoclinic symmetry (7) by 1.<sup>25,32</sup> However, this does not suggest an oxygen deficiency in the sample, since no difference in chemistry is accompanied, as will be shown in the XPS results (Figure 4). Also, it does not suggest a possible formation of a less-oxygen-coordinated local Magnéli structure such as those in the rutile or anatase phase of TiO<sub>2</sub>.<sup>33</sup> The 8-fold-coordinated tetragonal local structure of the Hf ions is confirmed by examining the Hf 5d electronic structure with

the O K-edge XAS (section 3.3). Therefore, the apparent inconsistency should be attributed to the strong structural disorders in the no-ozone sample, which could lower the FT magnitudes.<sup>24</sup>

The clear difference in the crystal structure after PDA between the no-ozone sample and the others [Figure 2b] further implies that the atomic distributions in the as-grown no-ozone sample cannot be completely the same as those in the other as-grown samples. If the atomic distributions were identical before PDA, the thermal atomic migrations should result in the same atomic distributions after PDA, contrary to the experimental results. Therefore, the difference that must be responsible for the structural transition during PDA, somehow should reside in the as-grown samples despite the similar local structures near the Hf atoms (Figure 2a). It will be suggested in sections 3.4 and 4.3 that C–O bonds remaining between the HfO<sub>2</sub> domains play a major role in the phase transition.

**3.3. O K-Edge XAS.** The local structure can be examined also by O K-edge XAS. O K-edge XAS reflects an unoccupied O 2p electronic density of states (DOS) with an O 1s core hole. Since the unoccupied O 2p DOS is largely determined by the unoccupied orbital states of the metal ions through the metal–oxygen orbital hybridization, O K-edge XAS is frequently used to examine the projected DOS of the metal orbital states, which is determined by the crystal fields of the oxygen coordination.<sup>34,35</sup> Therefore, the oxygen coordination of the metal ions can be inferred from their local electronic structures (i.e., O K-edge XAS spectra). Figure 3 shows the spectra for all of the

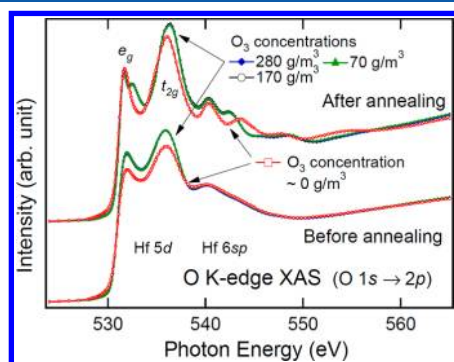


**Figure 3.** O K-edge X-ray absorption spectroscopy (XAS) of the HfO<sub>2</sub> films, manifesting a tetragonal local structure in no-ozone sample after annealing in contrast to the monoclinic-like local structures in other samples.

samples before and after PDA. The Hf orbital states can be assigned according to the photon energy range; the features below the photon energy of 540 eV are attributed to Hf 5d states, while those above are attributed to Hf 6sp and higher quantum states.<sup>25</sup> The spectra are normalized as to have the same height at the featureless high-energy regions.

For the samples before annealing, the spectra show broadened features compared with the samples after the annealing. This has been regarded typically as the consequence of structural disorders in the amorphous samples.<sup>34</sup> The spectra of the 70, 170, and 280 g/m<sup>3</sup> samples are almost identical either before or after PDA, while those of no-ozone samples are different, consistent to all of the results shown in this work. All the spectra of the samples before annealing are quite consistent with the previous reports on the amorphous HfO<sub>2</sub> with monoclinic-like local structures.<sup>34</sup> The slight decrease in the Hf 5d intensity in the case of the no-ozone sample *before* annealing

might be due to additional structural disorders, which would reduce the hybridization strength and, therefore, the O K-edge XAS intensity.<sup>36</sup> Since Hf 5d states are more localized than the Hf 6sp states, the decrease in intensity should occur especially for the Hf 5d features in the normalized spectrum.

The spectra of the 70, 170, and 280 g/m<sup>3</sup> samples after PDA show the typical line shapes of monoclinic HfO<sub>2</sub>, while that of the no-ozone sample after PDA shows the line shape of the tetragonal phase.<sup>25</sup> If the Hf–O coordination is 8-fold as in the tetragonal phase, the resultant electronic states should be split by a doublet  $e_g$  at a lower energy and a triplet  $t_{2g}$  at a higher energy because of the  $D_{2d}$  site symmetry.<sup>25</sup> In contrast, if the Hf–O coordination were 6-fold having an octahedral local structure ( $O_h$  symmetry), such as in the rutile or anatase phase, the triplet ( $t_{2g}$ ) should have lower energy than the doublet ( $e_g$ ).<sup>37</sup> It is clearly shown in Figure 3 that the lowest energy peak has a lower intensity than the next-lowest energy peak. This means that the lowest energy peak should be attributed to the  $e_g$  state, suggesting that the spectrum represents the  $D_{2d}$  symmetry as in ZrO<sub>2</sub> ( $P4_2/nmc$ ).<sup>25</sup> Therefore, the Hf–O coordination must be 8-fold. Then, the apparent decrease of the FT magnitude of the first shell in Figure 2 should be attributed to the enhanced structural disorders.<sup>35</sup> Features of the C–O bonds could also be shown in the high-energy region of the O K-edge XAS spectra.<sup>38</sup> However, its influence would be negligible since the amount of O–C bonds is small compared with that of the O–Hf bonds ( $\leq 5\%$ ).

Therefore, it has been clearly shown that the no-ozone sample is amorphous, having monoclinic-like local structures before the annealing similarly to other samples, while it crystallizes into a tetragonal phase after PDA, in contrast to the other samples. In the next section and in section 4, the stabilization mechanism of the tetragonal structure under an ozone-deficient environment and the role of the PDA will be discussed.

**3.4. Core-Level XPS.** The chemistries of the HfO<sub>2</sub> films are investigated by XPS.<sup>39</sup> Because of the short inelastic mean free paths of the photoelectrons, the probing depth of the XPS (with Al K $\alpha$  source) is less than 5 nm.<sup>40</sup> Since the thickness of the films is approximately 13 nm, the XPS does probe the film or film surface, not the HfO<sub>2</sub>/Si interface. The survey scan of XPS revealed that only Hf, O, and C exist in the films [within the range of detectable atomic species (other than H or He)]. Their respective core-level spectra are shown in Figure 4(a–c). Because the electron counts were collected using the same

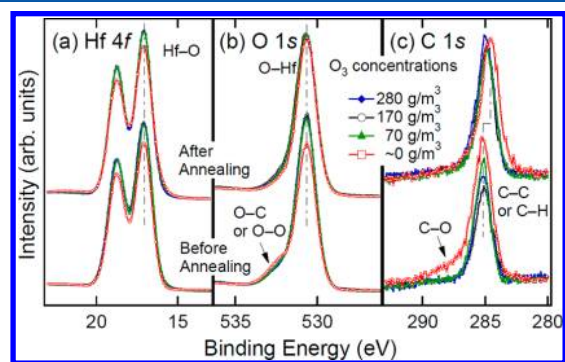


**Figure 4.** (a) Hf 4f, (b) O 1s, and (c) C 1s X-ray photoelectron spectroscopy (XPS) spectra of the HfO<sub>2</sub> films. The signatures of C–O bonds are clearly observed only in the spectra of the no-ozone sample before annealing (b and c).

photon source with the same collection time, the intensities of peaks can be compared directly within each core level.

In the case of Hf 4f and O 1s core levels (Figure 4a and b), no difference in the binding energies (BE) of the main peaks was observed for all samples before and after PDA, as shown by the vertical guidelines. This reflects nearly identical chemistry in the HfO<sub>2</sub> films, with +4 (Hf) and -2 (O) valences for all samples.<sup>18</sup> Besides the small shoulder at BE = 532–533 eV in Figure 4b, the main peaks of the 70, 170, and 280 g/m<sup>3</sup> ozone samples are almost identical, while those of the no-ozone samples showed a little decrease in intensity compared with the other samples. If the decrease in intensity were somehow related to the difference in the oxygen stoichiometry, either the Hf 4f or O 1s intensity (and also BE) should decrease while the other increases.<sup>18,41</sup> The stoichiometry of the HfO<sub>2</sub> film estimated by the XPS intensities of the main peaks of Hf 4f and O 1s and the atomic sensitivity factors will be shown in Figure 8. The almost constant stoichiometry ( $x$  in HfO <sub>$x$</sub> ) (Figure 8) as well as the constant BEs in Figure 4a and b, indicates that lack of ozone hardly influences the chemistry in the HfO<sub>2</sub> domains. Thus, the decrease in the Hf 4f and O 1s peak intensities while maintaining the stoichiometry should be understood as a signature of decrease in the density of the HfO<sub>2</sub> domains inside the film. The tendency of the film density examined by XRR will be shown in the next section. When the ozone is not supplied sufficiently, the Hf-precursors would be oxidized fully in some parts but not fully in some other parts so that some carbon atoms would remain after the oxidation step. Hence, it is possible that some carbon atoms would intervene between nearly perfect HfO<sub>2</sub> domains under the no-ozone condition preventing the densification of the HfO<sub>2</sub> layers. These might contribute to the C 1s peak as shown in Figure 4c. A tiny lower-BE shoulder is observed at BE ~16 eV in the Hf 4f peaks (Figure 4a) in the case of the no-ozone sample after PDA, reflecting a tiny influence of the oxygen deficiency in the HfO<sub>2</sub> domains.<sup>42</sup>

Some adhesions of dirt on the HfO<sub>2</sub> surface (e.g., during the exposure to the ambient air between the growth process and the XPS measurement) might also contribute to the decrease in the Hf 4f and O 1s peak intensities. Since they are mostly hydrocarbons, they should contribute to the C 1s XPS peak for the C–C or C–H bonds (BE ~285 eV) as well.<sup>43</sup> The C 1s main peaks of the as-grown samples show no tendency with increasing ozone concentrations, implying that they are influenced also by surface contaminations.<sup>44</sup> However, the contamination effect cannot explain all the observed tendency of the Hf 4f and O 1s intensities with the ozone concentration because there is no reason why the adhesion would be severe for the no-ozone samples. Further, it might be irrelevant to the phase transition to the tetragonal phase after PDA as discussed in the previous sections, since the adhesion reaction occurs at the surface only, so that it is hard to invoke the structural transition throughout the sample.

The total concentration of the C atoms in the samples deduced from the peak intensity and the atomic sensitivity factor, were at most 5% of the HfO<sub>2</sub>. It appears that the intensities of the C 1s main peaks (C–C or C–H bond) are overall larger for the samples after PDA compared with the as-grown samples. The larger intensities might originate not only from the migration of carbon atoms from deep inside the film to the surface but also from an additional adhesion of hydrocarbons during the PDA. The BEs of the C 1s main peaks also show a behavior that could be related to the

interaction at the C/HfO<sub>2</sub> interface, as shown by the guidelines in Figure 4c. They remain constant before annealing, while they decrease by 0.3 eV in the case of 70, 170, 280 g/m<sup>3</sup> samples and by 0.6 eV in the case of no-ozone sample. If the hydrocarbons at the film surfaces were purely physisorbed, no BE shifts of the C 1s main peaks should have been observed. Thus, the BE shifts implies a possible chemical reaction between the hydrocarbon layer and the HfO<sub>2</sub> film surface, which could show contrast in the BEs depending on the details in the morphology or the atomic structures at the interfaces. Interestingly, it is shown that the BE of the main peak is correlated with crystal structure, although the origin of the correlation is yet to be understood at this moment.

In the case of the no-ozone samples, a small but clear peak in the higher-BE shoulder of the O 1s peak at BE = 532–533 eV is observed before annealing, while it disappears after annealing (see Figure 4b). According to the O 1s BE, this shoulder peak can be attributed to the O–C or O–O bonds, which should reside out of the HfO<sub>2</sub> domains.<sup>45</sup> A higher-BE shoulder peak is also observed in the C 1s peak of the no-ozone sample only, and it disappears after PDA. This strongly suggests that the origins of the two shoulders are identical (i.e., the C–O bonds). Absence of such shoulders in other samples suggests that the C–O bonds originate from the remaining carbonates in the film under the condition of no-ozone, not from the surface contamination. The disappearance of the C–O bonds after PDA suggests that the carbonates should come out of the HfO<sub>2</sub> layers up to the surface or atmosphere during PDA. The stabilization of the tetragonal phase under the no-ozone condition after PDA considering the role of the C–O bonds in the HfO<sub>2</sub> films will be discussed further in section 4.3.

**3.5. XRR: Film Density.** The intervention of C atoms between the HfO<sub>2</sub> domains will decrease the density of the films. This tendency was truly observed in the reflectometry analysis. Figure 5 shows the specular reflectance data of the no-

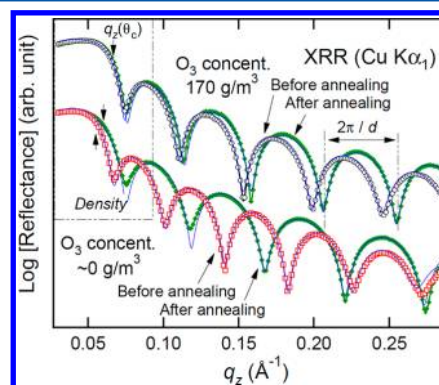


**Figure 5.** X-ray reflectometry (XRR) data of no-ozone and 170 g/m<sup>3</sup> (standard) samples before and after annealing as a function of perpendicular momentum transfer ( $q_z$ ) with the simulated data. The fitting parameters for the film thickness and density are listed in Table 1. A clear discrepancy in the lowest- $q_z$  features evidence the smaller mass density in the case of the no-ozone sample before annealing.

ozone and 170 g/m<sup>3</sup>-ozone samples before and after PDA as a function of the momentum transfer perpendicular to the sample surface ( $q_z$ ), which is equivalent to the value of  $4\pi \sin \theta$  divided by the X-ray wavelength. Assuming homogeneity in the HfO<sub>2</sub> film, the bulk information of the films, such as the thickness, mass density, and surface roughness, can be deduced from the data independently. First, the mass density can be

determined by the critical angle of the total reflection ( $\theta_c$ ), which is slightly before the steepest slope in the lowest  $q_z$  (see the dotted box in Figure 5).<sup>46</sup> The film thickness can be estimated by  $2\pi/\Delta q_z$  where  $\Delta q_z$  is the difference in the  $q_z$  values of neighboring intensity minima in the limit of large  $q_z$ , as shown in the figure.<sup>46</sup> Finally, the roughness of the layers can be measured by the abruptness of the decrease in reflectance with increasing  $q_z$ .<sup>46</sup> The overall similarity in the intensity between the XRR data, even at large  $q_z$ , indicates that the surface roughness of the samples is similar. The values of the mass densities and thicknesses obtained by the fittings (shown as solid lines in Figure 5), are listed in Table 1. Here a simple

**Table 1. Mass Densities, Film Thicknesses, and Layer Densities of Selected Samples Obtained by Fitting the X-ray Reflectometry Data (Figure 5) with a Simple Three-Layer Model (HfO<sub>2</sub>, an Interfacial Si-Oxide Layer, and the Si Substrate)**

O <sub>3</sub> (g/m <sup>3</sup> )	annealing (PDA)	mass density (g/cm <sup>3</sup> )	thickness (nm)	layer density (μg/cm <sup>2</sup> )
0	before PDA	5.9	14.3	8.4
	after PDA	6.3	11.8	7.4
170 (standard)	before PDA	7.3	13.2	9.6
	after PDA	7.5	12.7	9.5

three-layer model, in which the samples consist of the HfO<sub>2</sub> layer, an interfacial Si-oxide layer, and the Si substrate, was employed. The values for the Si substrate were set as a mass density of 2.328 g/cm<sup>3</sup>, infinite thickness, and zero surface roughness. The fitting results showed that the mass densities, thicknesses, and roughnesses of the interfacial Si-oxide layers are maintained as <2.2 g/cm<sup>3</sup>, ~3 nm, and ~0.2 nm, respectively, for all samples. Although the values might vary significantly depending on the layer models used in the simulation, the tendencies between the samples themselves should be definite. The values for the 70 and 280 g/m<sup>3</sup> samples were similar to those of the standard (170 g/m<sup>3</sup>) sample both before and after PDA.

It is clearly shown in Table 1 that the mass densities of the no-ozone samples are smaller than the standard (170 g/m<sup>3</sup>) samples by ~20%. This means that the HfO<sub>2</sub> layers in the no-ozone samples cannot be “pure.” In section 3.2, it was shown that the local structure (i.e., bond length) in the HfO<sub>2</sub> domains is similar to the other samples before PDA. Therefore, the reduced mass density must indicate an existence of a large void between the HfO<sub>2</sub> domains, which could be surrounded by some element other than Hf or O. This is consistent to our main arguments on the C atoms in the films. After PDA, the mass density increases toward the values of the standard samples, implying a partial reduction of the void or driving out the light atoms. The densification of the films, thus, should be understood as a process of purification, not a contraction of bonds.<sup>47</sup>

The film thickness of the no-ozone sample is slightly higher than that of the standard sample *before* PDA (+8%). This reflects a loose packing of the HfO<sub>2</sub> domains in the no-ozone sample. However, the thickness of the no-ozone sample becomes smaller than that of the standard *after* PDA (−7%). This suggests that the efficiency of the ALD is degraded under an insufficient ozone environment. It is further shown in Table 1 that the layer density, which is the mass density multiplied by the film thickness, is lower than the value of the standard (170

g/m<sup>3</sup>) samples when the samples were grown under no-ozone environment. Hence, it can be understood that the high thickness of the no-ozone sample before PDA is achieved because of the remaining impurities from the ligands, despite the low growth-rate under the ozone-deficient environment. The significant decrease in the layer density of the no-ozone sample after PDA (compared with the no-ozone sample before PDA), suggests that even some Hf and O atoms are driven out of the sample due to some bonding instability under incomplete ligand substitution.

**3.6. Valence and Conduction Bands.** Figure 6 shows the valence band (VB) spectra obtained by the XPS for all samples.

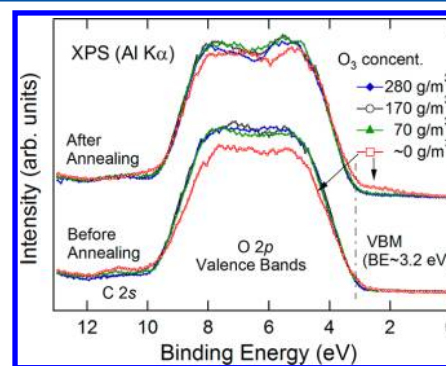


**Figure 6.** Valence band (VB) X-ray photoelectron spectroscopy (XPS) spectra of the HfO<sub>2</sub> films. An in-gap state is shown above the VB maximum (VBM) energy in the spectrum of the no-ozone sample after annealing.

The VBs comprise mainly O 2p states, while the small features at BE ~11 eV comprise the C 2s states.<sup>48</sup> The relatively small O 2p intensities of the no-ozone samples reflect the low density of oxygen atoms, consistent with the O 1s core levels in Figure 4b. The VB maximum (VBM) can be obtained by extrapolating the steepest slopes near the bandgap to the baseline.<sup>25</sup> All the VBM remain at BE ~3.2 eV, which means that the Fermi level is ~3.2 eV higher than the VBM for all cases, except for the formation of in-gap states in the case of the no-ozone samples. The in-gap state is further promoted after PDA, suggesting that the thermal treatment might aggravate the electrical performance of the high k films. The origin of the in-gap state is not clear. Most probably, it could originate either from the carbon atoms or HfO<sub>2</sub> in the film. A metallic state can be formed by carbon chains in the HfO<sub>2</sub> layers. The feature of C 2s state is not shown at BE ~11 eV, in the case of the no-ozone sample after PDA. This might originate from a BE shift toward the VBM, which can result in a nonlocal conduction by the C 2p states. Alternatively, the Hf 5d metallic states of the HfO<sub>2</sub> domains themselves can be promoted according to the oxygen deficiency.<sup>34</sup> Then the in-gap state might be correlated to the tiny lower-BE shoulder (BE ~16 eV) observed in the Hf 4f peaks (Figure 4a).

The conduction band (CB) spectra obtained by the O K-edge XAS are also shown in Figure 7, (a) before and (b) after PDA. Since the O K-edge XAS shows the unoccupied O 2p states only, the possible conduction through the C 2p states cannot be reflected in Figure 7. The CB minimum (CBM) in the HfO<sub>2</sub> domains can also be obtained by extrapolations as shown by arrows in the figure. For the case of the 70, 170, 280 g/m<sup>3</sup> samples, the CBM energy is reduced by ~0.3 eV after PDA, in contrast to the constant VBM (Figure 6). For the no-

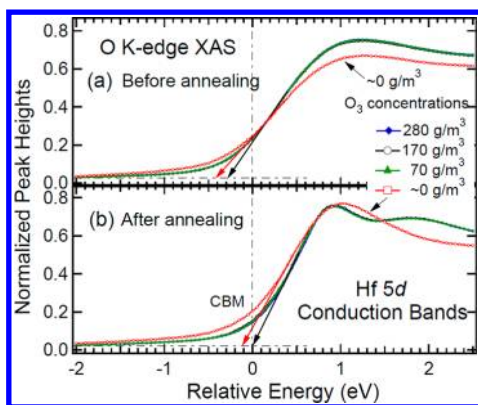


**Figure 7.** Conduction band (CB) structures of the HfO<sub>2</sub> films (a) before and (b) after annealing, taken from the low energy parts in the O K-edge X-ray absorption spectroscopy (XAS) spectra (Figure 4). Besides the disorder-induced broadening of features in the spectra of amorphous HfO<sub>2</sub> in (a), it is observed that the CB minima (CBM) are 0.1 eV lower than the other samples in the case of the no-ozone samples both before and after annealing.

ozone samples, only an additional decrease of CBM by ~0.1 eV was observed either before or after PDA. Along with the conducting carbon paths, the effectively reduced bandgap would be responsible for the higher leakage currents in the case of the no-ozone samples.

## 4. DISCUSSION

**4.1. Roles of Oxygen Source.** The primary role of the oxygen source is undoubtedly to supply the oxygen atoms into the Hf-precursor layer. Figure 8 shows the oxygen stoichiometry

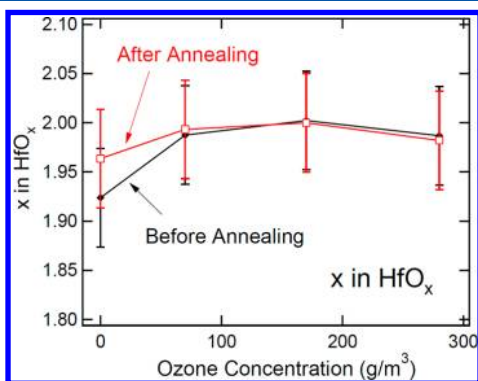


**Figure 8.** Relative oxygen concentration ( $x$ ) in the HfO <sub>$x \approx 2$</sub>  domains before and after annealing deduced from the core-level X-ray photoelectron spectroscopy (XPS) main peak intensities. Even in the absence of external ozone supply, the  $x$  is close to the stoichiometric value of 2, implying the nontrivial effect in the oxidation process.

tries of the samples before and after PDA deduced from the core-level XPS main peak intensities (section 3.4); therefore, it represents the number ratio of the oxygen atoms to the Hf atoms only in the HfO<sub>2</sub> domains. The error bars account for the uncertainty in the deduction of the XPS peak areas and in the atomic sensitivity factors (~5% of the mean value).<sup>45</sup> The relative concentration ratios ( $x$  in HfO <sub>$x$</sub> ) between the O and Hf atoms remain almost 2 within the error bars for all samples, although they decrease slightly as the ozone concentration decreases. This is consistent with the constant Hf–O

coordination number in the HfO<sub>2</sub> domains shown in section 3.2. The almost constant oxygen contents suggest that the structural distinction cannot be made solely by the stoichiometry in the HfO<sub>2</sub> domains themselves. Actually, if the number of the oxygen atoms outside the HfO<sub>2</sub> domains are also considered, the ratio,  $x$ , would increase further in the case of the no-ozone sample before PDA (due to the O–C bonds), so that the difference in the  $x$  values between the samples would be even smaller. This again implies that the structural transition is irrelevant to the oxygen contents in the film.

Meanwhile, it is suggested in section 3.4 that the C–O bonds reside between the HfO<sub>2</sub> domains only in the no-ozone sample before PDA because of the insufficient ligand removal. The difference in the C 1s binding energy (BE) between the C–O bonds and C–C or C–H bonds (partly from contamination at the topmost layers) implies that the C–O bonds should reside below the topmost layers. The possible atomic structures, in which such C–O bonds can exist in the HfO<sub>2</sub> layer, is described in a schematic diagram in Figure 9a. The Hf–O coordination is

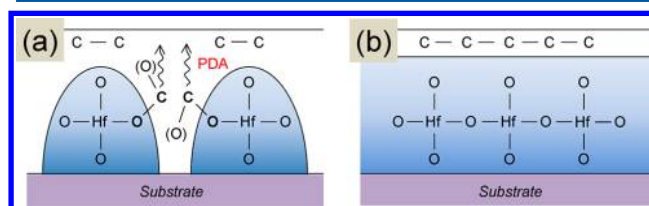


**Figure 9.** Schematic diagrams of the HfO<sub>2</sub> films grown by the atomic layer deposition. (a) In case of an insufficient oxidation, the C atoms from the ligands form the C–O bonds that intervene between the nanoscale HfO<sub>2</sub> domains, which might stabilize the tetragonal structures in the HfO<sub>2</sub> layers after postdeposition annealing (PDA). The C–O bonds disappear after annealing to aggregate the domains of tetragonal HfO<sub>2</sub>, apparently similar to panel b. (b) In the case of sufficient oxidation, large HfO<sub>2</sub> domains might form so that the monoclinic structure is stabilized after the PDA.

depicted as 4-fold only for simplicity. The C–O bonds might form if the C atoms are chemically bound at the O-terminated boundaries of the HfO<sub>2</sub> domains. Alternatively, the C–O bonds can also form with oxygen atoms that reside somehow outside the HfO<sub>2</sub> domains, as shown in parentheses in Figure 9(a). It should be noted that such atomic distributions (HfO<sub>2</sub> domains + intervening C) would form only under an extremely ozone-deficient condition. For the samples grown under the sufficient ozone concentrations (70, 170, and 280 g/m<sup>3</sup>), absence of such C–O bonds will result in an agglomeration of HfO<sub>2</sub> domains as depicted in Figure 9(b). However, this does not mean that the HfO<sub>2</sub> layers should be in a crystalline domain; the structures of the HfO<sub>2</sub> domains are amorphous (see section 3.3) so that the joint of the two domains does not mean much. Therefore, it can be concluded that the oxygen source not only conveys the oxygen atoms but also plays a role in removing the C–O bonds out of the sample so as to make large HfO<sub>2</sub> domains as shown in Figure 9b. Perhaps the O<sub>2</sub> gas also has potential to form the HfO<sub>2</sub> domains in the films grown by the atomic layer deposition, but (almost) complete removal of carbon atoms can be achieved only by the more active ozone gas.

**4.2. Roles of Postdeposition Annealing.** During PDA, the thermal energy enables the system to overcome the barriers for the crystallization. Therefore, it is natural that the films crystallized after PDA (Figure 1). Also, it activates the reactions at the surface so that ambient gas can interact actively with the

atoms at the film surface. Depending on the ambient condition during PDA, the oxygen contents could either increase or decrease. In Figure 8, a slight improvement in the stoichiometry is shown after PDA in the case of the no-ozone samples, while negligible effects were shown in the cases of other samples. Thus, the PDA “healed” the oxygen deficiency in the film slightly.

The more important point is that the C–O bonds in the no-ozone sample disappeared after PDA. The carbon atoms that contributed the C–O bonds [Figure 9a] could be reduced successfully by accompanying the “healing” of the HfO<sub>2</sub> domains during PDA. The reduced carbon atoms might be driven out of the sample or accumulated at the film surface, contributing the C–C or C–H bonds at the topmost layers. Therefore, it is clearly shown that the PDA removed the C–O bonds between the HfO<sub>2</sub> domains. The densification will be achieved through partial reduction of the voids in the film accordingly.

#### 4.3. Stabilization Mechanism of Tetragonal Phase.

Bulk pure hafnia (HfO<sub>2</sub>) possesses a monoclinic (*P*2<sub>1</sub>/*c*) crystal structure as its most stable phase. However, a tetragonal phase is also favored when the system is incorporated by doping of exotic atoms with ionic radii smaller than Hf (such as Al or Ti) or by a (local) epitaxial stabilization with a TiO<sub>2</sub> substrate.<sup>32,49,50</sup> This study showed that the tetragonal phase can be also stabilized by the insufficient ozone concentration even without the doping or substrate effects. The correlation between the ozone concentration and the crystal structure after PDA can be understood by adopting the knowledge on a martensitic transition in ZrO<sub>2</sub> nanostructures.<sup>51</sup> The nanosized ZrO<sub>2</sub> domains prefer to have a tetragonal crystal structure instead of having a monoclinic structure that has lower bulk free energy.<sup>35</sup> This has been attributed to relatively large contributions of the surface free energies in the nanostructures, which might have lower value in the case of tetragonal structure compared to the monoclinic structure. However, it has been understood that this does not happen in HfO<sub>2</sub>, probably because the surface contribution might be relatively small due to larger grain sizes in comparison with ZrO<sub>2</sub>.<sup>52,53</sup> However, if exotic atomic species (ad hoc, carbon) intervene in the HfO<sub>2</sub> layer, the layer would become comprised of the nanoscale domains (grains) whose sizes would not be achievable by normal ALD process. This was clearly confirmed by the observation of the microstructure of the film as shown below.

Figure 10 shows the cross-section TEM images for the ~10 nm-thick HfO<sub>2</sub> films grown with ozone concentrations of (a and b) 0 g/m<sup>3</sup> and (c) 170 g/m<sup>3</sup> after PDA. Figure 10a and c are taken in the HR mode, while b was taken with a lower magnification. The HfO<sub>2</sub> film grown with the ozone concentrations of 170 g/m<sup>3</sup> shows a normal microstructure having densely packed well-crystallized grains (red square region in Figure 10c) with an average grain size of 30–40 nm. The fast Fourier transformation (FFT) images, which correspond to the diffractograms of the HRTEM images showed that the crystal structure was monoclinic corroborating the XRD data. However, the HfO<sub>2</sub> films grown with the ozone concentrations of 0 g/m<sup>3</sup> showed a highly unusual microstructure; it is comprised of very fine (<~ 5–10 nm in diameter) grains with intervening amorphous-like regions. The FFT images showed several diffraction spots which cannot be assigned to monoclinic phase but a phase more close to the tetragonal (or cubic) structure. Therefore, the evolution of the no-ozone HfO<sub>2</sub> film into the nonmonoclinic phase during the

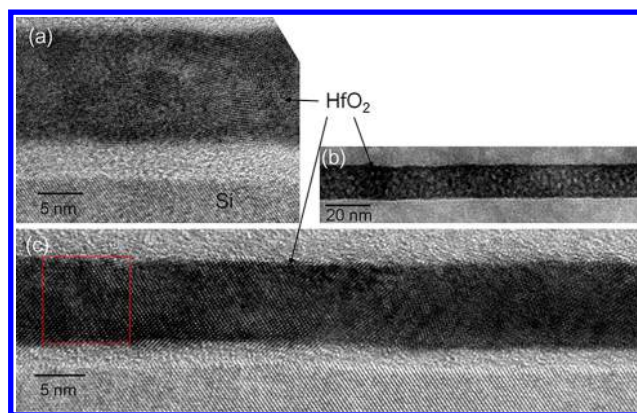


**Figure 10.** Cross-section TEM image of ~10 nm-thick HfO<sub>2</sub> films grown with ozone concentrations of (a, b) 0 g/m<sup>3</sup>, and (c) 170 g/m<sup>3</sup> after the PDA. The film grown with ozone concentrations of 0 g/m<sup>3</sup> shows very small crystalline grains with intervening amorphous regions, while the film grown with ozone concentrations of 170 g/m<sup>3</sup> showed a microstructure with densely packed relatively large grains.

PDA was ascribed to the much smaller size of the crystalline grains (or domains) which was induced by the involvement of impurities (C–O bonds).

It is noteworthy that the local structure of the no-ozone sample before PDA is monoclinic-like. The monoclinic-like local atomic structure was also found in the amorphous ZrO<sub>2</sub> thin films before PDA, which changed to the tetragonal structure after PDA.<sup>35</sup> In the amorphous films, there should be large positive contributions from the structural disorders to the bulk entropy of the system, so that this might lead to the preference of a monoclinic-like local structure again, as in the bulk material.<sup>35</sup> The monoclinic-like local structure in no-ozone HfO<sub>2</sub> film before PDA can be stabilized by the same mechanism. The nanosized HfO<sub>2</sub> domains should undergo the martensitic transition to the tetragonal crystallites during PDA. However, the other samples (70, 170, 280 g/m<sup>3</sup>) have no C–O bonds, thus, should have larger domains as in Figure 9(b). Thus, the monoclinic structure will be favored after PDA for these cases. Therefore, the intervention of carbon atoms and the formation of C–O bonds in the as-grown states are essential to induce the stabilization of the tetragonal structure of the HfO<sub>2</sub> domains after PDA. Hence, the apparent contradiction between the local structural similarity in the as-grown samples and the structural difference (tetragonal and monoclinic) after PDA is resolved by considering the role of C interventions.

In this work, it has been demonstrated that the remaining C atoms play a major role in the stabilization of the tetragonal phase. The dependence of atomic-scale orders on the ozone concentration was originated from the evident correlation with the efficiency of oxidation of the Hf-precursors. Therefore, a similar effect would be expected if the temperature is tuned during the ALD; a tetragonal phase should form (after PDA) when the film is grown at a lower temperature than the standard (280 °C). This was indeed observed in the authors' recent works.<sup>16,23</sup> It is consistent with this work overall, in that the C atoms exist before PDA, and a tetragonal phase is formed after PDA when the films were grown under insufficient oxidation. However, the details of resultant atomic structures in the low-temperature-grown HfO<sub>2</sub> films seem to be different from those in the low-ozone-grown films (this work). In the former case, the specimen was in a significant lack of oxidation

so that N atoms as well as a higher level of C atoms from the Hf-precursors were observed in the XPS measurements. It was proposed that the oxygen vacancy coupled with the C atoms in the HfO<sub>2</sub> domains can stabilize the tetragonal structure.<sup>16</sup> In contrast, all of the samples examined in this work have the same level of oxygen concentration (Figure 8), and the local structures in the as-grown samples do not vary depending on the ozone concentrations significantly (Figure 2). This suggests that the samples in this study were not in such an extreme condition as in the former study. The samples had structures that consisted of “pure” HfO<sub>2</sub> domains and intervening C atoms (Figures 9 and 10). At this moment, it is hard to estimate the influence of the C–O bonds *outside* the pure HfO<sub>2</sub> domains on the structural properties *in* the domains quantitatively. Further theoretical studies are required to clarify this issue.

## 5. CONCLUSION

Approximately 13 nm-thick HfO<sub>2</sub> films were grown on Si substrate by an atomic layer deposition technique under different ozone concentrations at a fixed temperature of 280 °C. The crystalline structure, local bonding structure, and chemistry of the film were quite similar to each other when ozone was supplied, while they are distinctive when only O<sub>2</sub> gas was flown during the oxygen source pulse step. When HfO<sub>2</sub> film is grown under the no-ozone environment, some C–O bonds remain between “pure” HfO<sub>2</sub> domains because of the incomplete ligand substitutions by oxidation. The carbonate bonds prevent the agglomeration of the nanoscale domains so as to stabilize a tetragonal structure after annealing by forming a smaller grain size. The ozone gas and annealing eliminate the residual carbonate bonds to form large-scale grains of monoclinic HfO<sub>2</sub>.

## AUTHOR INFORMATION

### Corresponding Author

\*E-mail: zax@snu.ac.kr (D.-Y.C.); cheolsh@snu.ac.kr (C.S.H.)

### Notes

The authors declare no competing financial interest.

## ACKNOWLEDGMENTS

This work is supported by the Convergent Research Center Program (2012K001299) through the National Research Foundation of Korea funded by the Ministry of Education, Science, and Technology (MEST). The experiments at the Pohang Light Source were supported partly by MEST and POSTECH.

## REFERENCES

- (1) Wilk, G. D.; Wallace, R. M.; Anthony, J. M. *J. Appl. Phys.* **2001**, *89*, 5243.
- (2) <http://www.intel.com/content/dam/doc/guide/gate-dielectric-scaling-for-cmos-guide.pdf> (accessed Sep. 5, 2012).
- (3) Sherman, A. *Atomic Layer Deposition for Nanotechnology*; Ivoryton Press: Ivoryton, CT, 2008.
- (4) Ritala, M.; Leskelä, M. In *Handbook of Thin Film Materials*, Vol. 1; Nalwa, H. S., Ed.; Academic Press: San Diego, CA, 2001; pp 103–156.
- (5) Houssa, M., Ed. *High k Gate Dielectrics*, Series in Material Science and Engineering; Institute of Physics: Philadelphia, PA, 2004.
- (6) Gusev, E. P., Ed. *Defects in High-k Gate Dielectric Stacks: Nano-Electronic Semiconductor Devices*; Springer: New York, NY, 2006.
- (7) Gutowski, M.; Jaffe, J. E.; Liu, C.-L.; Stoker, M.; Hegde, R. I.; Rai, R. S.; Tobin, P. J. *J. Appl. Phys. Lett.* **2002**, *80*, 1897.
- (8) Ribes, G.; Mitard, J.; Denais, M.; Bruyere, S.; Monsieur, F.; Parthasarathy, C.; Vincent, E.; Ghibaudo, G. *IEEE Trans. Device Mater. Reliab.* **2005**, *5*, S–19.
- (9) Peacock, P. W.; Robertson, J. *Phys. Rev. Lett.* **2004**, *92*, 57601.
- (10) Cho, M.; Jeong, D. S.; Park, J.; Park, H. B.; Lee, S. W.; Park, T. J.; Hwang, C. S.; Jang, G. H.; Jeong, J. *J. Appl. Phys. Lett.* **2004**, *85*, 5953.
- (11) Triyoso, D. H.; Hegde, R. I.; White, B. E.; Tobin, P. J. *J. Appl. Phys.* **2005**, *97*, 124107.
- (12) Schaeffer, J.; Edwards, N. V.; Liu, R.; Roan, D.; Hradsky, B.; Gregory, R.; Kulik, J.; Duda, E.; Contreras, L.; Christiansen, J.; Zollner, S.; Tobin, P.; Nguyen, B.-Y.; Nieh, R.; Ramon, M.; Rao, R.; Hegde, R.; Rai, R.; Baker, J.; Voight, S. J. *Electrochem. Soc.* **2003**, *150*, F67–F74.
- (13) Takahashi, K.; Funakubo, H.; Hino, S.; Nakayama, M.; Ohashi, N.; Kiguchi, T.; Tokumitsu, E. *J. Mater. Res.* **2004**, *19*, S84–S89.
- (14) Cho, M.; Degraeve, R.; Pourtois, G.; Delabie, A.; Ragnarsson, L.-A.; Kauerauf, T.; Groeseneken, G.; de Gendt, S.; Heyns, M.; Hwang, C. S. *IEEE Trans. Electron Devices* **2007**, *54*, 752.
- (15) Cho, M.; Kim, J. H.; Hwang, C. S.; Ahn, H.-S.; Han, S.; Won, J. Y. *J. Appl. Phys. Lett.* **2007**, *90*, 182907.
- (16) Jung, H. S.; Jeon, S. H.; Kim, H. K.; Yu, I.-H.; Lee, S. Y.; Lee, J.; Chung, Y. J.; Cho, D.-Y.; Lee, N.-I.; Park, T. J.; Choi, J.-H.; Han, S.; Hwang, C. S. *ECS J. Solid State Sci. Technol.* **2012**, *1*, N33–N37.
- (17) Park, J.; Park, T. J.; Cho, M.; Kim, S. K.; Hong, S. H.; Kim, J. H.; Seo, M.; Hwang, C. S.; Won, J. Y.; Jeong, R.; Choi, J.-H. *J. Appl. Phys.* **2006**, *99*, 094501.
- (18) Cho, D.-Y.; Min, C.-H.; Kim, J.; Oh, S.-J.; Kim, M. G. *J. Appl. Phys. Lett.* **2006**, *89*, 253510.
- (19) Kim, J. H.; Park, T. J.; Cho, M.; Jang, J. H.; Seo, M.; Na, K. D.; Hwang, C. S.; Won, J. Y. *J. Electrochem. Soc.* **2009**, *156*, G48–G52.
- (20) Ho, M.-Y.; Gong, H.; Wilk, G. D.; Busch, B. W.; Green, M. L.; Voyles, P. M.; Muller, D. A.; Bude, M.; Lin, W. H.; See, A.; Loomans, M. E.; Lahiri, S. K.; Räisänen, P. I. *J. Appl. Phys.* **2003**, *93*, 1477.
- (21) Mukhopadhyay, A. B.; Musgrave, C. B.; Sanz, J. F. *J. Am. Chem. Soc.* **2008**, *130*, 11996–12006.
- (22) Park, T. J.; Kim, J. H.; Jang, J. H.; Kim, U. K.; Lee, S. Y.; Lee, J.; Jung, H. S.; Hwang, C. S. *Chem. Mater.* **2011**, *23*, 1654–1658.
- (23) Jung, H.-S.; Kim, H. K.; Yu, I.-H.; Lee, S. Y.; Lee, J.; Park, J.; Jang, J. H.; Jeon, S.-H.; Chung, Y. J.; Cho, D.-Y.; Lee, N.-I.; Park, T.-J.; Choi, J.-H.; Hwang, C. S. *J. Electrochem. Soc.* **2012**, *159*, G33–G39.
- (24) Cho, D.-Y.; Park, T. J.; Na, K. D.; Kim, J. H.; Hwang, C. S. *Phys. Rev. B* **2008**, *78*, 132102.
- (25) Cho, D.-Y.; Jung, H.-S.; Hwang, C. S. *Phys. Rev. B* **2010**, *82*, 094104.
- (26) Zhao, X.; Vanderbilt, D. *Phys. Rev. B* **2002**, *65*, 233106.
- (27) Boscke, T. S.; Muller, J.; Brauhuis, D.; Schroder, U.; Bottger, U. *J. Appl. Phys. Lett.* **2011**, *99*, 102903.
- (28) Mueller, S.; Mueller, J.; Singh, A.; Riede, S.; Sundqvist, J.; Schroeder, U.; Mikolajick, T. *Adv. Funct. Mater.* **2012**, DOI: 10.1002/adfm.201103119.
- (29) Garcia, J. C.; Scolfaro, L. M. R.; Leite, J. R.; Lino, A. T.; Freire, V. N.; Farias, G. A.; da Silva, E. F., Jr. *J. Appl. Phys. Lett.* **2004**, *85*, 5022.
- (30) Stern, E. A.; Newville, M.; Ravel, B.; Yacoby, Y.; Haskel, D. *Phys. Rev. B* **1995**, *52*, 208–209, 117.
- (31) Park, T. J.; Chung, K. J.; Kim, H.-C.; Ahn, J.; Wallace, R. M.; Kim. *Electrochem. Solid-State Lett.* **2010**, *13*, G65–G67.
- (32) Lee, C.-K.; Cho, E.; Lee, H.-S.; Hwang, C. S.; Han, S. *Phys. Rev. B* **2008**, *78*, 012102.
- (33) Kwon, D.-H.; Kim, K. M.; Jang, J. H.; Jeon, J. M.; Lee, M. H.; Kim, G. H.; Li, X.-S.; Park, G.-S.; Lee, B.; Han, S.; Kim, M.; Hwang, C. S. *Nat. Nanotechnol.* **2010**, *5*, 148–153.
- (34) Cho, D.-Y.; Lee, J.-M.; Oh, S.-J.; Jang, H.; Kim, J.-Y.; Park, J.-H.; Tanaka, A. *Phys. Rev. B* **2007**, *76*, 165411.
- (35) Cho, D.-Y.; Jung, H.-S.; Kim, J. H.; Hwang, C. S. *J. Appl. Phys. Lett.* **2010**, *97*, 141905.
- (36) Cho, D.-Y.; Kim, J. H.; Na, K. D.; Song, J.; Hwang, C. S.; Park, B.-G.; Kim, J.-Y.; Min, C.-H.; Oh, S.-J. *J. Appl. Phys. Lett.* **2009**, *95*, 261903.
- (37) Kucheyev, S. O.; van Buuren, T.; Baumann, T. F.; Satcher, J. H., Jr.; Willey, T. M.; Meulenber, R. W.; Felner, T. E.; Poco, J. F.; Gammon, S. A.; Terminello, L. J. *Phys. Rev. B* **2004**, *69*, 245102.
- (38) Yang, B. X.; Kirz, J.; Sham, T. K. *Phys. Lett.* **1985**, *110A*, 301–304.

- (39) Wang, Y.; Wang, H.; Zhang, J.; Wang, H.; Ye, C.; Jiang, Y.; Wang, Q. *Appl. Phys. Lett.* **2009**, *95*, 032905.
- (40) Tanuma, S.; Powell, C. J.; Penn, D. R. *Surf. Sci. Lett.* **1987**, *192*, L849.
- (41) Cho, D.-Y.; Oh, S.-J.; Chang, Y. J.; Noh, T. W.; Jung, R.; Lee, J.-C. *Appl. Phys. Lett.* **2006**, *88*, 193502.
- (42) Cho, D.-Y.; Park, K.-S.; Choi, B.-H.; Oh, S.-J.; Chang, Y. J.; Kim, D. H.; Noh, T. W.; Jung, R.; Lee, J.-C.; Bu, S. D. *Appl. Phys. Lett.* **2005**, *86*, 041913.
- (43) Johnston, E. E.; Ratner, B. D. *J. Electron Spectrosc. Relat. Phenom.* **1996**, *81*, 303–317.
- (44) Ye, C.; Wang, Y.; Zhang, J.; Zhang, J.; Wang, H.; Jiang, Y. *Appl. Phys. Lett.* **2011**, *99*, 182904.
- (45) Moulder, J. F. ; Stickle, W. F.; Sobol, P. E. ; Bomben, K. D. *Handbook of X-ray Photoelectron Spectroscopy*, 2nd ed.; Physical Electronics, Inc.: Chanhassen, MN, 1995.
- (46) Daillant, J.; Gibaud, A., Ed.; *X-ray and Neutron Reflectivity, Principles and Applications Series*; Springer: New York, NY, 2009.
- (47) Olivier, S.; Duc  r  , J. M.; Mastail, C.; Landa, G.; Est  ve, A.; Rouhani, M. D. *Chem. Mater.* **2008**, *20*, 1555–1560.
- (48) H  chst, H.; Steiner, P.; H  fner, S.; Politis, C. *Z. Phys. B* **1980**, *37*, 27–31.
- (49) Seo, M.; Kim, S. K.; Min, Y.-S.; Hwang, C. S. *J. Mater. Chem.* **2011**, *21*, 18497–18502.
- (50) Seo, M.; Kim, S. K.; Han, J. H.; Hwang, C. S. *Chem. Mater.* **2010**, *22*, 4419.
- (51) Tang, J.; Zhang, F.; Zoogman, P.; Fabbri, J.; Chan, S.-W.; Zhu, Y.; Brus, L. E.; Steigerwald, M. L. *Adv. Funct. Mater.* **2005**, *15*, 1595–1602.
- (52) Hedge, R. I.; Triyoso, D. H.; Samavedam, S. B.; White, B. E., Jr. *J. Appl. Phys.* **2007**, *101*, 074113.
- (53) Jung, H.-S.; Jang, J. H.; Cho, D.-Y.; Jeon, S.-H.; Kim, H. K.; Lee, S. Y.; Hwang, C. S. *Electrochem. Solid-State Lett.* **2011**, *14*, G17–G19.

#### ■ NOTE ADDED AFTER ASAP PUBLICATION

This article was published ASAP on September 6, 2012, with minor errors in the References section. The correct version was published ASAP on September 7, 2012.